

3D Atomic Mapping of Interfacial Roughness and Its Spatial Correlation Length in Sub-10 nm Superlattices

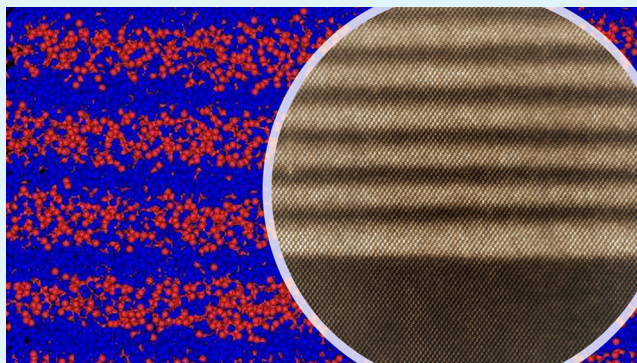
Samik Mukherjee,*†^{ID} Anis Attiaoui,[†] Matthias Bauer,[‡] and Oussama Moutanabbir*,[†]^{ID}

[†]Department of Engineering Physics, École Polytechnique de Montréal, C. P. 6079, Succ. Centre-Ville, Montreal, Québec H3C 3A7, Canada

[‡]Applied Materials Inc., 974 E. Arques Avenue, Sunnyvale, California 94085, United States

Supporting Information

ABSTRACT: The interfacial abruptness and uniformity in heterostructures are critical to control their electronic and optical properties. With this perspective, this work demonstrates the three-dimensional (3D) atomic-level mapping of the roughness and uniformity of buried epitaxial interfaces in Si/SiGe superlattices with a layer thickness in the 1.5–7.5 nm range. Herein, 3D atom-by-atom maps were acquired and processed to generate isoconcentration surfaces highlighting local fluctuations in content at each interface. These generated surfaces were subsequently utilized to map the interfacial roughness and its spatial correlation length. The analysis revealed that the root-mean-squared roughness of the buried interfaces in the investigated superlattices is sensitive to the growth temperature with a value varying from 0.17 ± 0.02 to 0.26 ± 0.03 nm in the temperature range of 500–650 °C. The estimated horizontal correlation lengths were found to be 8.11 ± 0.5 nm at 650 °C and 10.09 ± 0.6 nm at 500 °C. Additionally, reducing the growth temperature was found to improve the interfacial abruptness, with a 30% smaller interfacial width is obtained at 500 °C. This behavior is attributed to the thermally activated atomic exchange at the surface during the heteroepitaxy. Finally, by testing different optical models with increasing levels of interfacial complexity, it is demonstrated that the observed atomic-level roughening at the interface must be accounted for to accurately describe the optical response of Si/SiGe heterostructures.



KEYWORDS: silicon–germanium superlattices, atom probe tomography, interfacial roughness, interface correlation length, interfacial width, spectroscopic ellipsometry

1. INTRODUCTION

Heterostructures have been a rich platform to engineer a variety of low-dimensional structures and devices.^{1–6} In such systems, the nature of the interfaces is a crucial factor that ultimately defines their basic properties and performance. For instance, it is well-known that several terahertz to infrared sources and detectors operate on the basis of intersubband transitions across semiconductor quantum wells, wherein the linewidth of these transitions depends strongly on the interface roughness.^{7,8} This becomes more prominent in quantum cascade structures where the electronic states are spread out over several quantum wells and encompass several interfaces whose roughness is not correlated.^{4,7} The spatial correlation of the vertical height distribution of buried epitaxial interfaces is an important parameter to evaluate the performance of quantum cascade structures because it underlies crucial information required to evaluate the scattering matrix.⁹ In fact, the interface roughness in a cascaded structure induces intersubband scattering between electronic states when the correlation length matches the inverse of the momentum needed for the process. However, despite their importance,

direct measurements of the horizontal correlation length for the buried interfaces are still conspicuously missing in the literature. As a matter of fact, this correlation length is currently used as a fitting parameter to theoretical models.¹⁰ Additionally, the precise knowledge of the roughness of buried interfaces has also become increasingly critical in silicon (Si) gate-all-around designs recently introduced for the 7 nm technology node and beyond.¹¹ These architectures are based on Si/SiGe superlattices (SLs) where selective wet-etching of the SiGe layers is used to release the Si layers and form vertically stacked Si nanosheets. The Si/SiGe interfacial width and irregularities before the etching are expected to determine the roughness of Si nanosheets and hence the extent of charge carrier surface scattering and the overall performance of the final device. The control of the interfacial abruptness and the thickness uniformity has also implications in the development of Si-based direct bandgap semiconductor materials by

Received: August 3, 2019

Accepted: December 6, 2019

Published: December 6, 2019

Table 1. Composition, Layer Thickness, and Roughness of $(\text{Si})_m/(\text{Si}_{1-x}\text{Ge}_x)_m$ Samples Measured with AFM, APT, HR-STEM, HRXRD, and SE

sample no.	mean x in $\text{Si}_{1-x}\text{Ge}_x$ ^a	mean period thickness in nm ^a from						mean period thickness from HR-STEM (nm)	Surface RMS roughness (nm) from AFM, over $(10 \times 10) \mu\text{m}^2$ scan area		
		HR-STEM ^b		HRXRD		SE ^c					
		$\text{Si}_{1-x}\text{Ge}_x$	Si	$\text{Si}_{1-x}\text{Ge}_x$	Si	$\text{Si}_{1-x}\text{Ge}_x$	Si				
S-3	0.31 ± 0.05	7.6 ± 0.2	6.3 ± 0.2	11.2	9.5	8.4 ± 0.9	6.5 ± 0.7	13.9 ± 0.3	0.44		
S-6	0.26 ± 0.05	5.4 ± 0.3	4.2 ± 0.2	5.6	4.9	5.7 ± 0.9	4.5 ± 1.6	9.6 ± 0.4	0.53		
S-12	0.25 ± 0.05	2.4 ± 0.2	2.0 ± 0.1	2.4	2.4	1.2 ± 0.7	1.8 ± 0.9	4.2 ± 0.2	0.55		
S-16	0.25 ± 0.05	2.2 ± 0.3	1.3 ± 0.2	1.9	1.8	2.5 ± 0.5	1.6 ± 0.8	3.5 ± 0.4	0.64		

^aThe mean includes the last $\text{Si}_{1-x}\text{Ge}_x$ layer, which had grown thicker and with higher Ge content than the remaining $\text{Si}_{1-x}\text{Ge}_x$ layers. The Ge content was estimated from APT measurements and not HRXRD. ^bThickness obtained by fitting the HAADF intensity profile with Gaussians. ^cThe M_{int}^{σ} optical model was used to estimate the average thicknesses of the $\text{Si}_{1-x}\text{Ge}_x$ and Si layers in the SLs.

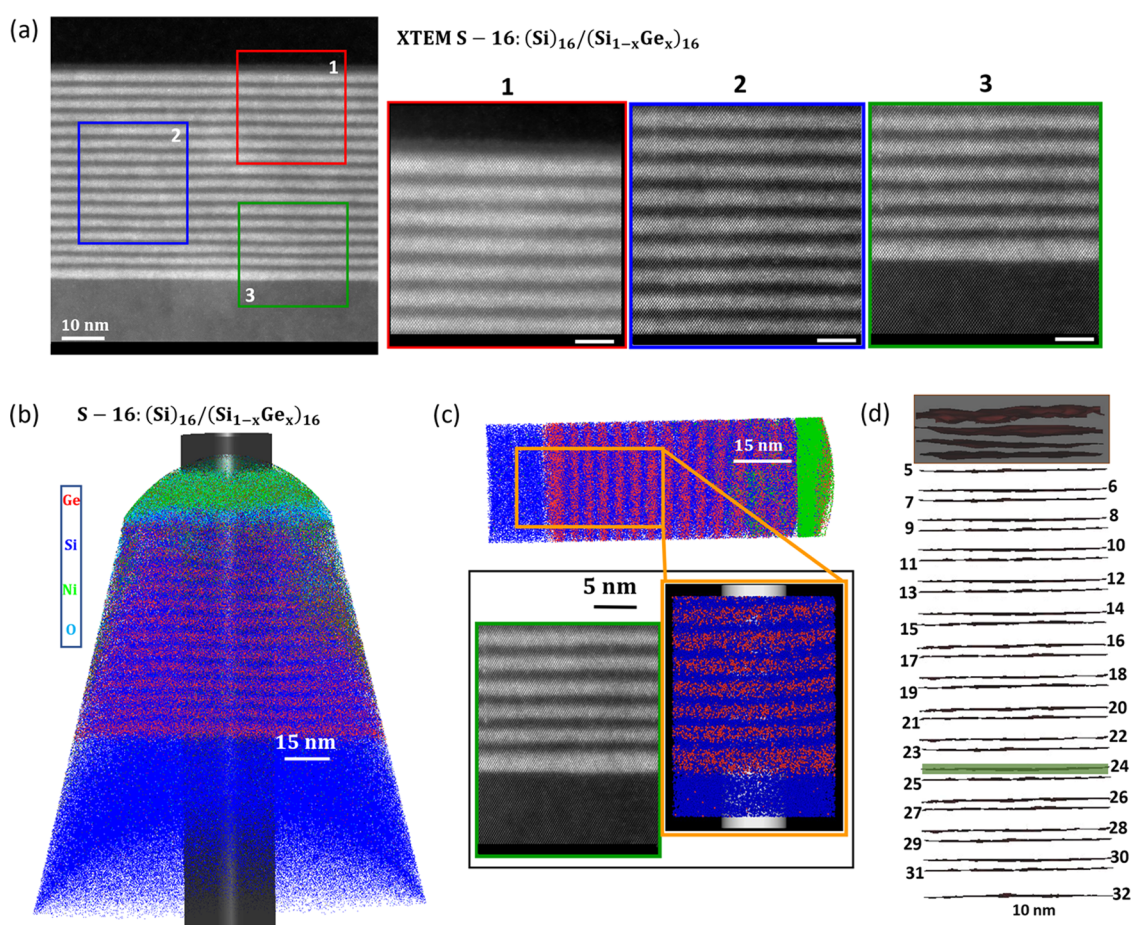


Figure 1. HAADF images and APT 3D reconstruction of sample S-16. (a) HAADF image of sample S-16. Zoom into the selected regions of the image is shown alongside using the numbered boxes. All scale bars for the images within these boxes correspond to 5 nm. (b) 3D atom-by-atom APT reconstruction of sample S-16. (c) Top: 3D reconstruction of the atoms lying within the black cylinder (diameter 30 nm) at the center of the 3D reconstruction shown in (b). Bottom: comparison demonstrating the correspondence of the HAADF image with the APT reconstruction, by zooming into the last (bottom-most) 6–7 periods of sample S-16. (d) Si/SiGe heterointerfaces of sample S-16, represented as Ge isoconcentration surfaces drawn within the reconstruction shown in the (c) top.

superimposing a periodic SL potential onto the crystal lattice potential.¹² A periodic sequence of a few atomic planes of Si and Ge leads to a new larger lattice constant in one direction, and, consequently, the Brillouin zone is reduced along this axis. A proper choice of the SL period length results in a Brillouin zone folding such that initially indirect conduction band

minima are shifted back to the center of the reduced Brillouin zone, giving rise to direct electronic transitions. Inevitably, the implementation of these photonic structures requires a meticulous control of the roughness and abruptness at each interface. The elements above highlight the importance of understanding the interfacial properties of epitaxial multilayer

structures. With this perspective, this work describes a method to achieve a three-dimensional (3D) atomic-level mapping of the roughness and uniformity of buried epitaxial interfaces in a variety of $(\text{Si})_m/(\text{Si}_{1-x}\text{Ge}_x)_m$ (" m " being the number of periods) SLs.

2. RESULTS AND DISCUSSION

The details of the growth of the SLs as well as the details of all of the analytical tools used in this work to characterize the SLs are provided in Section 4 (experimental details). The samples are labeled based on their periodicities, m . For example, the sample with 16 periods ($m = 16$) is named S-16 and so on. In addition to S-16, the other investigated samples are S-12, S-6, and S-3. S-16 and S-12 were grown at 650 °C, S-6 at 600 °C, and S-3 at 500 °C. The mean Ge concentration of the $\text{Si}_{1-x}\text{Ge}_x$ layers within the SLs is in the ~25 to ~30 atom % range, and their thickness varies from ~40 to ~60 nm (Table 1). Herein, high-resolution scanning transmission electron microscopy (HR-STEM) analysis and three-dimensional (3D) atom probe tomography (APT) are combined to elucidate the properties of heteroepitaxial interfaces (see details in Section 4). Spectroscopic ellipsometry (SE) models at increasing levels of complexity were developed to evaluate the impact of the interfacial sharpness on the optical response of the investigated heterostructures (see details in Section 4). Figure 1a shows the high-angle annular dark-field (HAADF) images of sample S-16. The HAADF image of other investigated SLs is shown in Figure S1 in the Supporting Information (SI). $\text{Si}_{1-x}\text{Ge}_x$ layers appear brighter than Si layers in the HAADF images in Figure 1a. The insets are zoom-in HAADF images of different regions in the SL. The $\text{Si}_{1-x}\text{Ge}_x/\text{Si}$ interfaces in the HAADF images appear to be coherent without the presence of any extended defects. The mean thickness of each $\text{Si}_{1-x}\text{Ge}_x$ and Si layer in different samples, as extracted from the HAADF images, is presented in Table 1. Table 1 also lists the layer thickness estimated from high-resolution X-ray diffraction (HRXRD) scans and SE. The SE estimation of the layer thickness has been presented later in the text. During the optimization process, after every sample growth (even those not discussed here), HRXRD scans were performed to get a quick estimate of the layer thicknesses, crystallinity, and the average Ge content within the SiGe layers, before the parameters for the next growth were chosen. The HRXRD scan results are not shown here, but to provide a comparison with the layer thicknesses extracted from the STEM analysis, the HRXRD-extracted layer thicknesses of each SL samples have been highlighted in Table 1. The table also shows the surface root-mean-squared (RMS) roughness of each SL sample obtained with an atomic force microscope (AFM). The RMS surface roughness was used to build the optical model for the SE data analysis. Figure 1b shows the 3D atom-by-atom reconstruction of SL S-16. Only one representative 3D reconstruction is shown. Out of all of the samples studied, S-16 possesses the highest number of interfaces and, therefore, provides the larger statistics on any interfacial parameter that is being measured. Hence, the APT investigations of the interface properties have been demonstrated in the following sections using this SL, but the same methodology was applied to investigate the interfacial properties in all of the other SLs. The evaporation of atoms being the most uniform from the center of an APT tip,¹³ only atoms from within the black cylinder (diameter 30 nm) at the center of the 3D reconstruction in Figure 1b were extracted and the corresponding 3D reconstruction is shown in Figure 1c.

top. Note that as the 3D reconstruction in APT can often be subjected to artifacts as far as the length scales of features are concerned. Thus, the correlation with STEM analysis has been followed to optimize the APT reconstruction parameters, as shown in Figure 1c-bottom. The APT reconstruction of all samples investigated in this work was done iteratively until the layer thickness of the 3D APT reconstruction matches (with 5.0% tolerance) to that obtained from the corresponding HAADF image. Furthermore, 2–3 tips from each sample were analyzed in APT to gather better statistics and verify the sample uniformity.

The estimated average Ge concentration within the $\text{Si}_{1-x}\text{Ge}_x$ layers is 24.5 ± 0.5 atom % (see the one-dimensional (1D) concentration profile from APT and its associated discussion later in the text). The bottom-most $\text{Si}_{1-x}\text{Ge}_x$ layer, which grew thicker than the rest of the layers, possesses a relatively higher Ge concentration of ~30.0 atom %. The mean Ge contents of the $\text{Si}_{1-x}\text{Ge}_x$ layers, as extracted from APT, are given in Table 1. Figure 1d shows the buried $\text{Si}/\text{Si}_{1-x}\text{Ge}_x$ interfaces, drawn as isoconcentration surfaces within the 3D reconstruction (shown in Figure 1c, top) defined at 50% of the mean Ge concentration in the $\text{Si}_{1-x}\text{Ge}_x$ layers. The interface number increases in the direction of the APT evaporation sequence. In the next section, the roughness and spatial correlation have been extracted for these interfaces, defined as isoconcentration surface. Clearly, the top 3–4 interfaces (enclosed within the partially transparent black rectangular box in Figure 1d) were slightly damaged during the FIB preparation and have been omitted from the analysis. The method implemented to extract the RMS roughness and horizontal correlation length is explained by randomly selecting interface number 24 (marked by the green rectangle in Figure 1d) as an example. First, the interface properties were exported and the vertical height (z) at every point over the interface (defined as isoconcentration surfaces) was evaluated and plotted as a color-coded image, as shown in the inset of Figure 2a. The height–height correlation function $H(\tau)$ is the squared difference in height of two points (x,y) and (x',y') separated by a distance τ and is given by $H(\tau) = \langle |z(x,y) - z(x',y')|^2 \rangle$, where $z(x,y)$ is the height of the interface at the position (x,y) , relative to a mean plane, and $\tau = [(x - x')^2 + (y - y')^2]^{1/2}$.^{14,15} For a pixelated color-coded image like the one in the inset of Figure 2a, the following equation was used to calculate the correlation function

$$H(\tau) = \frac{1}{N'(M' - m')} \sum_{l'=1}^{N'} \sum_{n'=1}^{M'-m'} (z_{n'+m',l'} - z_{n',l'})^2 \quad (1)$$

where M' and m' are, respectively, the total number of pixels and the separation between two pixels on the image during a line scan along an arbitrarily chosen axis and N' is the total number of scan lines required to encompass the whole interface. The pixel size in the color-coded images is the grid parameter ($1.0 \text{ nm} \times 1.0 \text{ nm} \times 1.0 \text{ nm}$ voxel size) used during the 3D reconstruction. The evolution of $H(\tau)$ as a function of τ for interface number 24 (from top) of sample S-16 is shown in Figure 2a.

Phenomenologically, the height–height correlation can be fitted by the function $H_{\text{fit}}(\tau) = 2\sigma^2[1 - e^{-(\tau/\xi)^{\alpha}}]$, where σ is the RMS roughness, ξ is the horizontal correlation length, and α is called the Hurst parameter.^{14,15} The data in Figure 2a was fitted with the function $H_{\text{fit}}(\tau)$ (red line) to estimate the parameters σ and ξ . It is clear from Figure 2a that $H(\tau)$ exhibits two distinct regimes. First, a linear increase where

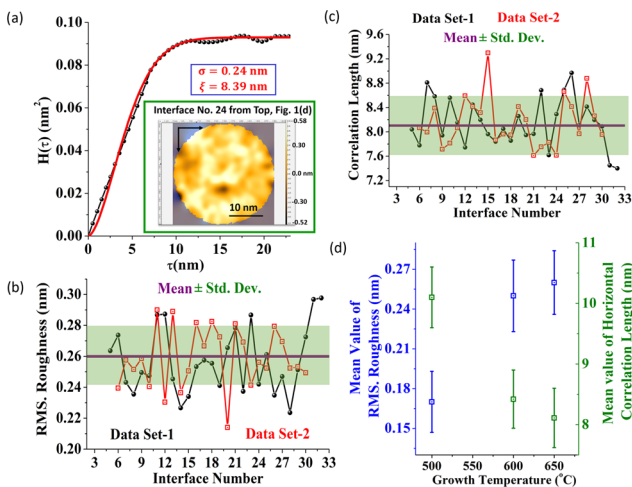


Figure 2. Extraction of the RMS. roughness and horizontal correlation length. (a) The evolution of height–height correlation function with the horizontal length of interface 24 in Figure 1d and the corresponding fitting function (red). The color-coded height distribution of the same interface is shown in the inset. For the convenience of the display, some of the values of the color bar have been highlighted. The extracted value of RMS roughness (σ) and the horizontal correlation length (ξ) for interface 9 of sample S-16 are highlighted in the inset. The accuracy of the fit or the R^2 value was found to be better than 0.99. (b) The extracted values of σ of all of the interfaces of sample S-16 over two different data sets. For data set-2 of sample S-16, the top 6 interfaces were damaged from Ga ion implantation and the tip fractured while transiting through the last $\text{Si}_{1-x}\text{Ge}_x$ layer. Hence, the data for interface number 7 to 30 are shown. (c) The extracted values of ξ of all of the interfaces of sample S-16 over two different data sets. In (b) and (c), the mean value of σ and ξ is shown using the thick purple line and the uncertainty (shown using the green transparent box) represents the standard deviation of the data. (d) Evolution of σ (in blue) and ξ (in green) of the SLs as a function of the growth temperature. The error bars represent the standard deviation over all of the interfaces and over different data sets of a sample.

$H(\tau)$ strongly depends on the value of τ , implying a strong correlation between any two points situated at (x,y) and (x',y') . Second, when $H(\tau)$ becomes independent of τ , it implies the loss of all correlations between any two points situated at (x,y) and (x',y') . The point of crossover from the first regime to the second, where the correlation function starts to flatten out, is the one that defines the horizontal correlation length ξ . For interface number 24 of S-16, σ of 0.24 nm and ξ of 8.39 nm were estimated from the fit. A similar example using a randomly selected interface of sample S-3 is shown in Figure S3. Figure 2b,c shows the values of σ and ξ of all of the interfaces over two different data sets of S-16, respectively. From the data, no meaningful differences can be observed between the interfaces at $\text{Si}_{1-x}\text{Ge}_x \rightarrow \text{Si}$ transitions and those at the reverse transition. The mean values of σ and ξ were found to be 0.26 ± 0.03 and 8.11 ± 0.5 nm, respectively. The uncertainty here is the standard deviation over all of the interfaces and over two different APT data sets. As shown in Figure S4, for sample S-6, the mean values of σ and ξ were found to be 0.25 ± 0.03 and 8.42 ± 0.5 nm, respectively, similar (within the uncertainty) to that of S-16. However, the mean values of σ and ξ for sample S-3 were found to be 0.17 ± 0.02 and 10.10 ± 0.6 nm, respectively, as evident from Figure S5. A graphical representation of the evolution of the mean

values of σ and ξ of the SLs as a function of the growth temperature is presented in Figure 2d.

A segment of the 1D concentration profile (at a fixed bin width of 0.2 nm) of the last 7 periods of sample S-16 is shown in Figure 3a. The profile in Figure 3a was collected from within

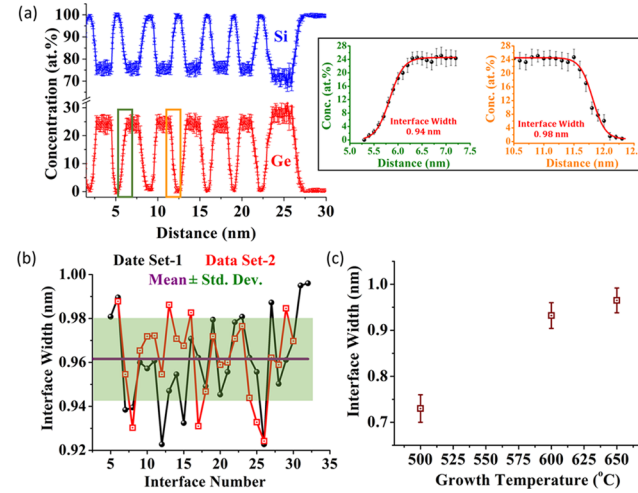


Figure 3. Extraction of interfacial width. (a) Concentration profiles of Si and Ge of the last 7 periods of sample S-16, recorded at a fixed bin width of 0.2 nm (from within the white cylinder of diameter 8 nm, within the APT reconstruction shown in Figure 1c, bottom). The interfaces marked by the orange and the green rectangles are used in the inset to demonstrate the extraction of the interfacial width. Inset: (Left) Zoom-in at the green rectangle at the 12th interface from the bottom, showing a rising Ge concentration and corresponding sigmoid fit (in red). The extracted value of the interface width is 0.95 nm. (Right) Zoom-in at the 9th interface from the bottom, showing a falling Ge concentration and corresponding sigmoid fit (in red). The extracted value of the interface width is 0.96 nm. The accuracy of the fit or the R^2 value for both the plots in the inset was found to be better than 0.99. (b) The interface width of all of the interfaces of sample S-16 over two different data sets. The mean value of the interface width is shown using the thick purple line, and the uncertainty (shown using the green transparent box) represents the standard deviation of the data. (c) Evolution of the mean interface width of the SLs as a function of the growth temperature. The error bars represent the standard deviation over all of the interfaces and over different data sets of a sample.

the white cylinder, placed at the center of 3D APT reconstruction in the inset of Figure 1c, bottom. The full 1D concentration profile of Si and Ge across all of the 16 interfaces, recorded from both APT and electron energy loss spectroscopy (EELS) data, is shown in Figure S2. A feature that showed up in all of the samples analyzed in this work is that the bottom-most SiGe layer was found to be slightly thicker with slightly higher Ge content, as compared to the rest. The bottom-most layer was the first layer to have grown, immediately after the Si substrate was baked at a high temperature. After the bake, the temperature was ramped down to the desired growth temperature. In all likelihood, the bottom-most SiGe layer in the samples grew when the temperature was still slightly higher than the growth temperature of the subsequent layer. The error bars in the concentration profiles in Figure 3a show IVAS-generated one-sigma statistical error, the magnitudes of which are $\sqrt{C_i(1 - C_i)/N}$, where C_i is the atomic fraction of the i th element within a bin and N is the total number of atoms within

a bin.¹⁶ The inset of Figure 3a shows the rising (top) and falling (bottom) Ge concentration profiles, zoomed into the 12th and the 9th interfaces from the bottom of the SL. In this work, rising ($\text{Si} \rightarrow \text{Si}_{1-x}\text{Ge}_x$ transition) and falling ($\text{Si}_{1-x}\text{Ge}_x \rightarrow \text{Si}$ transition) are denoted relative to the direction of evaporation in APT, which is opposite to the growth direction. The raw data was fitted using the sigmoid function

$$c(x) = c_0 + d_0/[1 + e^{-(x_0 \pm x)/\mathcal{L}}] \quad (2)$$

where c_0 is a vertical positioning parameter, x_0 is a horizontal positioning parameter, d_0 is a scaling parameter, and the parameter \mathcal{L} determines the value of the interface width.¹⁷ For the two interfaces shown in the inset of Figure 3a, interface widths were estimated to be 0.95 and 0.96 nm. The width of all of the interfaces (spread over 2 different data sets) of sample S-16, as extracted from APT, is shown in Figure 3b. Clearly, there is no difference between $\text{Si} \rightarrow \text{Si}_{1-x}\text{Ge}_x$ and $\text{Si}_{1-x}\text{Ge}_x \rightarrow \text{Si}$ transitions. Overall, the interface widths are randomly distributed with a mean value of 0.96 ± 0.02 nm. The 1D Ge concentration profile (binned at 0.2 nm) of sample S-6 is shown in Figure S6a. The average Ge concentration within the $\text{Si}_{1-x}\text{Ge}_x$ layers of sample S-6 is 24.4 ± 0.5 atom %. Figure S6b shows that the mean value of the interface widths in this SL is 0.94 ± 0.02 nm, close to that of SL S-16. However, SL S-3 exhibits a different behavior. The comparison of the 1D concentration profiles from APT and EELS for sample S-3 is shown in Figure S7a,b, respectively. The average Ge concentration within the $\text{Si}_{1-x}\text{Ge}_x$ layers of sample S-3 is about 30.70 ± 0.5 atom %. Figure S7c shows that the mean value of the interface width of sample S-3 (over 3 different data sets) is 0.73 ± 0.02 nm, about 30% smaller than that of S-16. A graphical comparison, showing the evolution of the interface width with the growth temperature of the samples, is displayed in Figure 3c.

The mean value of σ for S-3 is about 34% smaller, while the mean value of ξ is 24% larger as compared to that of S-16. The interface properties of sample S-6 (grown at 600 °C) are quite similar to that of sample S-16. As far as the interface widths are concerned, the data suggests that there is no Ge segregation during the Si overlayer growth atop the $\text{Si}_{1-x}\text{Ge}_x$ layers in any of the samples. The phenomenon of Ge segregation has long been thought to be one of the main processes limiting the realization of sharp interfaces with identical widths for both $\text{Si}_{1-x}\text{Ge}_x \rightarrow \text{Si}$ transition and the reverse transition.^{18,19} The fact that the width and roughness of the $\text{Si}_{1-x}\text{Ge}_x \rightarrow \text{Si}$ transitions are comparable to that of the reverse transitions indicates that Ge segregation is suppressed during the growth of SLs. Note that the rate of Ge surface segregation is often reduced when the growing surface is covered by some surfactant atoms like H or chlorine.²⁰ The surface H that is produced by the carrier gas as well as from the dissociation of disilane and germane on the growth front seems to be effective in preventing the Ge segregation. Bulk diffusion can be reasonably assumed to play an insignificant role since it is an energetically unfavorable process.^{21,22} The interface width for the samples investigated here might simply be determined by an atomic exchange process between the subsurface atoms and ad-atoms on the growing surface. This is a kinetically controlled surface phenomenon, with activation energies of a fraction of an eV.²³ In the absence of bulk diffusion, the atomic exchange in a surface layer halts when the subsequent growing layer sweeps across the entire surface. The analysis shows that

the interface roughness is more significant for a wider interface as compared to a relatively sharper interface. The buried interfaces are defined as isoconcentration surfaces, which were created in the first place by fitting the 3D atomic distribution (within each voxel) by polygons. More intermixing across the interfaces consequently leads to a larger uncertainty in placing polygons within each voxel, precisely at the predefined Ge concentration. The interfaces, defined as isoconcentration surface, which are nothing but a combination of all of these polygons, turn out to be rougher when compared to an interface with relatively less intermixing. In the following, the effects of this atomic-level roughening on the optical properties of the investigated SLs are discussed.

SE studies were first carried out to independently assess the thickness of the buried interfaces. The recorded optical response is shown here to provide a quantitative measure of the interfacial broadening in the investigated SLs. To build any ellipsometry model, an initial estimate of the thicknesses and composition of each layer is required. To this end, symmetric (004) and asymmetric (224) HRXRD spectra (not shown here) were measured for all SLs and fitted using standard dynamical simulations. HRXRD was used to ensure that the SE investigations of the SL interface widths are completely independent of any inputs from the HR-STEM analysis and APT. Table 1 displays a summary of the measurements conducted on different SLs. Note that SE-based analysis of the thickness shows a relative fluctuation between 24 and 46% when compared to the HAADF images. Figure 4a shows a layer-by-layer optical model (M_X) where the interfaces are simply omitted (i.e., no interfacial broadening). In contrast, Figure 4b illustrates a model where the interfacial layers have been incorporated (M_{int}). In brief, in the M_{int} model, the initial layer thicknesses $d_{\text{Si}}^{(i)}$ and $d_{\text{SiGe}}^{(i)}$ were obtained from HRXRD. All of the optical models take into account the Bruggeman effective medium approximation (B-EMA).^{24–28} The approximation combines the dielectric functions of two adjacent layers to form the dielectric constant of the interface. In the model labeled $M_{\text{int}}^{\text{1-EMA}}$, the dielectric constant of an interface was taken as a combination of the dielectric constants of Si and Ge. However, for $M_{\text{int}}^{\text{2-EMA}}$, a combination of the dielectric constant of $\text{Si}_{1-x}\text{Ge}_x$ and Si was used. In the $M_{\text{int}}^{\text{1-EMA}}$ model, EMA % represents the average Ge content within the host material Si. Third, a new parametric graded interfacial alloy model (M_{int}^{α}) was introduced where the Si content inside the interface layer is graded (described by eq 2), and the floating parameters are the scaling parameter d_0 (the average Ge concentration at the interface) and the interfacial width (labeled $d_{\text{int}}^{(i)}$ for the i th interface, in the optical models). An iterative process was developed to extract the desired set of parameters. The first iteration involved varying the layer thicknesses ($d_{\text{SiGe}}^{(i)}$ and $d_{\text{Si}}^{(i)}$) and keeping fixed the interface width ($d_{\text{int}}^{(i)}$). In the second iteration, each layer thickness was fixed and $d_{\text{int}}^{(i)}$ was varied. This iterative process is repeated until the mean-squared error (MSE, see Sections 3.1 and 3.2 for more details) between two consecutive steps is smaller than a set tolerance value of 10^{-3} and the gradient of $\Delta_{\text{Err}}^{\text{S-m}}$ (eq 3) is minimized. Knowing the optical properties of Si and $\text{Si}_{1-x}\text{Ge}_x$ thin layers are also required to implement the optical models. To this end, pseudomorphic $\text{Si}_{1-x}\text{Ge}_x$ layers with Ge content below 54% and a thickness between 19 and 33 nm were used to extract the optical properties of $\text{Si}_{1-x}\text{Ge}_x$ layers in the SLs.²⁹ Those of Si layers were evaluated from a reference sample consisting of a 12 nm thick silicon-on-insulator (SOI), which

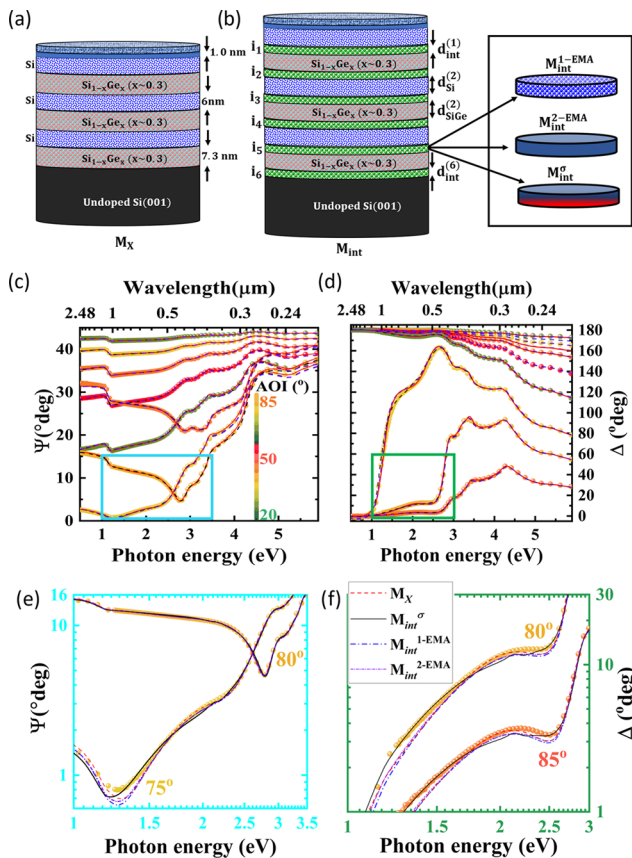


Figure 4. Different spectroscopic ellipsometric models used throughout this work and spectroscopic ellipsometry-measured parameters for sample S-6. (a) M_X is the HAADF image-based SE optical model where the layer-by-layer structure is the building block of the model. The thicknesses and the composition of Ge in each layer are evaluated. The schematic also incorporates a SiO_2 layer as well as a surface roughness layer (top layer), which are kept fixed during the optical modeling. (b) By adding an interfacial layer i_m between each Si and $\text{Si}_{1-x}\text{Ge}_x$ layers of the M_X model, with thickness $d_{\text{int}}^{(i)}$, the interface can be analyzed in all of the SLs. Inset: Three different methods are proposed to physically model the interface. The first $M_{\text{int}}^{1-\text{EMA}}$ consists of using a Bruggeman-EMA model where a physical mixture between Si and Ge is assumed, whereas in $M_{\text{int}}^{2-\text{EMA}}$ the interface is composed of a physical mixture between Si and $\text{Si}_{1-x}\text{Ge}_x$. Finally, a graded interfacial layer is also studied in the M_{int}^{σ} model where the Si content in the interface is determined by a sigmoid function as described in eq 2 in the text. (c) Ψ and (d) Δ extracted from the SE measurements. The fit to the experimental data based on the four optical models mentioned in the text (see the details of the optical models in the SI). (e) Zoom into the blue rectangle in (c) showing a log–log plot of the data in the spectral region from 1 to 3.5 eV. (f) Zoom into the green rectangle in (d) showing a log–log plot of the data in the spectral region from 1 to 3.0 eV. (e)–(f) provides visual confirmation of the superiority of the fit provided by the M_{int}^{σ} as compared to the others. The fit to the experimental data in (c)–(f) by the M_X , the $M_{\text{int}}^{1-\text{EMA}}$, and the $M_{\text{int}}^{2-\text{EMA}}$ optical models is shown using dashed lines (red, blue, and purple, respectively), while that by the M_{int}^{σ} model is shown using the black solid line.

was characterized for an angle of incidence (AOI) between 60 and 85° (see Figure S9). The full details of the aforementioned optical models are provided in Sections 3.1 and 3.2 of the SI.

Figure 4c,d exhibits the measured and fitted ellipsometric parameters Ψ and Δ , respectively, for S-6 at an AOI between 20 and 85°. Note that the same analysis was conducted for

other SLs as well. Overlaid in the same figure is the fit to the experimental parameters using the four different optical models described above. The dashed red, blue, and purple lines correspond to the M_X , $M_{\text{int}}^{1-\text{EMA}}$, and $M_{\text{int}}^{2-\text{EMA}}$ optical models, while the solid black line corresponds to the M_{int}^{σ} model. The difference between the optical models has been clearly shown in Figure 4e,f, using sample S-6 as an example. The fit was found to be excellent for all spectra with a MSE between 3.3 and 5.5 for the proposed models. Nonetheless, a closer inspection of the fitted spectra reveals a different observation. Indeed, Figure 4e,f, respectively, shows, in the log–log scale, the SE parameters Ψ and Δ at the high incidence angle ($\geq 75^\circ$) for a spectral range of interest where the most features in the data set are noticed (the blue and the green boxes within Figure 4c,d). Above 2.6 eV, almost all of the models accurately reproduce the experimental measurement, whereas below 2.6 eV, only the M_{int}^{σ} model (solid black line) mirrors the measured data set the best. This is further confirmed by comparing the obtained MSE of the four models, where the smallest MSE of 2.3 corresponds to M_{int}^{σ} . Figure 5a displays the variation of the

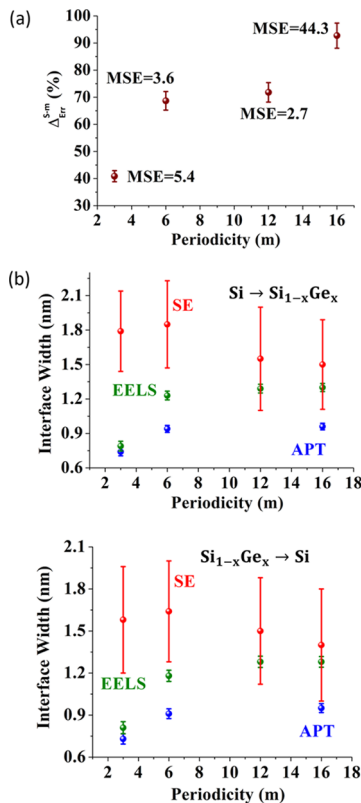


Figure 5. Comparison of the MSE and interface width across different SL samples measured using EELS, APT, and SE. (a) The variation of the average thickness relative error $\Delta_{\text{err}}^{\text{S}-\text{m}} (\%)$ as a function of the number of periods m evaluated from the M_X optical model. The MSE is also overlaid in the figure to show that even though the MSE is small, which is usually indicative of the accurate SE model, the error of the developed optical model is still high, thus justifying the necessity to use $\Delta_{\text{err}}^{\text{S}-\text{m}}$ as a metric to quantify the accuracy of the optical model, in addition to the MSE. (b) A comparison of the variation of the rising ($\text{Si} \rightarrow \text{Si}_{1-x}\text{Ge}_x$) and falling ($\text{Si}_{1-x}\text{Ge}_x \rightarrow \text{Si}$) interfacial width estimated from three different characterization techniques: red from SE, olive-green from EELS, and blue from APT. The error bar estimation for the SE data is the standard deviation evaluated from the iterative process.

Table 2. Quantitative Comparison of All of the Proposed Optical Models (M_X , $M_{int}^{1\text{-EMA}}$, $M_{int}^{2\text{-EMA}}$, and M_{int}^{σ}) where the First Column Shows the Behavior of the Average Thickness Relative Error $\Delta_{\text{Err}}^{S\text{-m}}$ (%) as a Function of the Studied Superlattices (S-m) and the Optical Model Used^a

model	$\Delta_{\text{Err}}^{S\text{-m}}$ (%)				Si \rightarrow $\text{Si}_{1-x}\text{Ge}_x$ interfacial width (nm)			Si $_{1-x}\text{Ge}_x \rightarrow$ Si interfacial width (nm)			
	sample	M_X	$M_{int}^{1\text{-EMA}}$	$M_{int}^{2\text{-EMA}}$	M_{int}^{σ}	$M_{int}^{1\text{-EMA}}$	$M_{int}^{2\text{-EMA}}$	M_{int}^{σ}	$M_{int}^{1\text{-EMA}}$	$M_{int}^{2\text{-EMA}}$	M_{int}^{σ}
S-3	41(2)	39(4)	40(1)	37(1)	2.6(1.6)	2.57(1.10)	1.48(0.50)	2.6(1.8)	2.35(0.85)	1.79(0.40)	
S-6	69(3)	43(3)	43(6)	22(1)	2.05(0.78)	2.37(0.57)	1.64(0.40)	2.74(0.70)	1.23(0.50)	1.86(0.46)	
S-12	72(4)	77(3)	51(3)	48(1)	2.26(0.95)	2.84(0.50)	1.45(0.35)	2.40(0.85)	2.80(0.40)	1.35(0.45)	
S-16	93(5)	85(2)	75(3)	32(2)	2.35(0.83)	2.62(0.45)	1.35(0.35)	2.54(0.35)	2.20(0.40)	1.26(0.40)	

^aThe second and third columns present the extracted $\text{Si}_{1-x}\text{Ge}_x \rightarrow$ Si and rising $\text{Si} \rightarrow \text{Si}_{1-x}\text{Ge}_x$ interfacial thickness for the interfacial optical models. The values in parenthesis represent the error associated with the values.

average thickness relative error $\Delta_{\text{Err}}^{S\text{-m}}$ (%) as a function of the number of periods m for the M_X model. $\Delta_{\text{Err}}^{S\text{-m}}$ is defined as follows:

$$\Delta_{\text{Err}}^{S\text{-m}} = 100 \times \sum_{i=1}^m \left| \frac{d_{\text{SE}}^{(i)} - d_{\text{HR-STEM}}^{(i)}}{d_{\text{HR-STEM}}^{(i)}} \right| \quad (3)$$

where $d_{\text{SE}}^{(i)}$ and $d_{\text{HR-STEM}}^{(i)}$ represent the SE- and the HR-STEM-extracted thickness of the i th layer, respectively. The small MSE values need to be cross-correlated to a small average relative error ($\Delta_{\text{Err}}^{S\text{-m}}$) to evaluate the accuracy of the model. In fact, even though the MSE values are relatively smaller for $m \leq 12$, which usually indicates a good fit quality and an accurate optical model, the $\Delta_{\text{Err}}^{S\text{-m}}$ is, in general, high for all of the SL samples. This is a clear indication that the M_X model overestimates the layer thicknesses in all investigated SLs, justifying the need for a more elaborate optical model. The first column of Table 2 shows in detail the systematic decrease in the error of the estimated layer thickness relative to the HR-STEM analysis. For instance, a reduction of $\Delta_{\text{Err}}^{S\text{-m}}$ from 72 to 51% is observed by adding the additional EMA interfacial layer for S-12. The same iterative routine was also used for the M_{int}^{σ} model. As a matter of fact, the M_{int}^{σ} model shows on average the smallest $\Delta_{\text{Err}}^{S\text{-m}}$ (36%) in comparison to the $M_{int}^{1\text{-EMA}}$ (62%) and $M_{int}^{2\text{-EMA}}$ (52%) models. This is a clear indication that the interfacial broadening must be considered for an accurate analysis of the optical response of the investigated SLs.

From Table 2, the rising and falling interfacial widths are higher than 2.0 nm for all SLs. Additionally, the Ge EMA atom % is very small (below 10 atom %) for the $M_{int}^{1\text{-EMA}}$ model, whereas it is above 50 atom % for the $M_{int}^{2\text{-EMA}}$ model. This discrepancy indicates that modeling the $\text{Si}_{1-x}\text{Ge}_x$ –Si interface as a mixture of two materials having different optical properties is likely an invalid approximation. Next, from the M_{int}^{σ} optical model, it is possible to estimate the Ge atom % at the interface, which corresponds to the variable d in eq 2. An average Ge content between 12.0 and 16.0 atom % was estimated for the falling interfacial layer ($\text{Si}_{1-x}\text{Ge}_x \rightarrow$ Si) for all SLs, while for the rising interfacial layer ($\text{Si} \rightarrow \text{Si}_{1-x}\text{Ge}_x$), the average Ge content was found to vary between 11.0 and 17.0 atom %. Furthermore, as shown in Figure 5b, the interfacial width obtained from the M_{int}^{σ} model gives a more accurate fit to the experimental data as compared to the EMA-based optical models. Figure 5b compiles the rising ($\text{Si} \rightarrow \text{Si}_{1-x}\text{Ge}_x$) and falling ($\text{Si}_{1-x}\text{Ge}_x \rightarrow$ Si) interfacial widths estimated from APT, EELS, and SE. It is interesting to highlight that the average relative differences between SE and EELS values of the rising and falling interfacial widths are 55 and 39%, respectively. This relative difference is much larger when SE is compared to APT. However, while the influence of the interface roughness on the

optical properties is clearly demonstrated here, it remains very challenging to precisely quantify this interfacial roughness using SE. The latter seems to always overestimate the interfacial broadening as compared to APT and EELS, but only by less than 1 nm. Note that this difference may perhaps come from the fluctuations associated with the lateral scale probed by each method.

3. CONCLUSIONS

In summary, by using Si/SiGe as a model system, APT-generated 3D maps of SLs and buried interfaces have been employed to quantify the interfacial roughness, and the height–height correlation length was obtained for a variety of sub-10 nm heterostructures. The analysis of isoconcentration maps revealed that the RMS roughness of the buried interfaces is sensitive to the growth temperature with the mean values varying from 0.17 to 0.26 nm, in the temperature range of 500–650 °C. For SLs grown at 500 °C, the RMS roughness was found to be ~30% smaller and the horizontal correlation length ~24% larger, as compared to those grown at 650 °C. A similar behavior was also observed for the interfacial abruptness, which was found to be practically identical for both $\text{Si} \rightarrow \text{Si}_{1-x}\text{Ge}_x$ and $\text{Si}_{1-x}\text{Ge}_x \rightarrow$ Si interfaces. These studies lay the groundwork to systematically investigate the effects of growth parameters (carrier gas, purging steps between the growth of different layers, different precursors and their partial pressures, material systems, etc.) on the properties of the buried interfaces and their effects on the overall performance. Finally, SE-based optical investigations revealed that an accurate analysis of the optical response of a multilayer heterostructure must take into account the broadening at the interface between different layers.

4. EXPERIMENTAL SECTION

4.1. Growth of the SL Samples. The latter were grown at different temperatures in a reduced pressure chemical vapor deposition reactor, on 300 mm undoped Si(001) wafers, using disilane and monogermane as precursors and hydrogen as the carrier gas.

4.2. High-Resolution Scanning Transmission Electron Microscopy. The sample preparation for APT and the HR-STEM analysis was performed in a Helios Nanolab 650 dual channel (Ga⁺ ion column for milling, SEM column for imaging) focused-ion beam (Dual-FIB) microscope, using the standard lamella lift-out technique. The HR-STEM analysis was conducted in a double cross-section-corrected FEI Titan microscope, operated at 200 kV, using a converge angle of 19.1 mrad. CEOS CESCOR corrector was used to yield a resolution of 0.8 Å. The images were recorded using a HAADF detector, and the data was processed using the digital micrograph GMS3 software. For the STEM-EELS analysis, the spectrometer entrance aperture was set to 5 mm, giving a collection semiangle of 55

mrad. The signal integration time was 5 ms. The spot size for the measurements was set to 9 nm. Aberration-corrected magnetic lenses helped in making the probes of the order of 1–2 Å diameter with a beam current of 250 pA. A dispersion of 1 eV/channel was used.

4.3. Atom Probe Tomography. Prior to the APT tip fabrication in Dual-FIB, a 50 nm thick Ni capping layer was co-deposited on all of the samples (using an electron-beam evaporator) to protect the top-most part of the samples from ion-implanted damage during the tip fabrication process. APT achieves electric field-induced evaporation of atoms as cations, in a layer-by-layer fashion, from the surface of a needle-like specimen, with the assistance of an ultrafast pulsed laser.^{30,31} In this work, the field evaporation of individual atoms in the APT was assisted by focusing a picosecond pulsed UV laser ($\lambda = 355$ nm), with a beam waist smaller than 5 μm , on the apex of the needle-shaped specimen. The laser pulse repetition rate was maintained at 500 kHz throughout. The evaporation rate (ion/pulse) and the pulse energy were varied over a single run. An APT run started with the onset of evaporation of Ni atoms from the capping layer. During this, an evaporation rate of 0.8–1.0 and a laser pulse energy of 30.0 pJ were maintained. As soon as the atoms from the SL appeared at the outer rim of the detector ion map, the evaporation rate was slowed down to 0.2 in a single step and the laser energy was lowered to 4.0–5.0 pJ, in steps of 1.0 pJ. The run was slowed down to ensure that the tip makes a gradual and smooth transition from the Ni cap into the SL without fracturing it. When all of the Ni atoms were evaporated and the transition into the SL was complete, the evaporation rate was slowly increased in small steps of 0.20 up to 1.0, ensuring in each step that the automatic voltage ramp is not too steep, a scenario which is well-known to cause tip fracture in APT. After the evaporation made a complete transition from the SL into the Si substrate, the rate was further increased (in steps, reaching up to 3.0–4.0) as well as the pulse energy (in steps, reaching up to 10–15 pJ) to collect a substantial amount of substrate atoms as quickly as possible before ending the run. The base temperature and base pressure within the APT chamber were maintained at 30 K and 3.2×10^{-11} Torr, respectively.

4.4. Spectroscopic Ellipsometry. Room-temperature pseudo-dielectric functions $\varepsilon(\omega) = \varepsilon_1(\omega) + i\varepsilon_2(\omega)$ were measured with an automatic rotating analyzer, variable angle spectroscopic ellipsometer.³² The samples were mounted and optically aligned with a He–Ne laser in a windowless cell. SE data were collected in the energy range of 0.5–6.0 eV with a 0.01 step size, using multiple angles of incidence (AOI), ranging from 20 to 85°. The Si substrate without the HF dip was also measured by SE under identical conditions to obtain reference data for bulk Si, which compared well with data from Palik.³³ Having a complete and precise structural characterization of the studied SLs is of paramount importance to build an accurate optical ellipsometry model. Indeed, when the optical constants or film structures of a sample are not known well, the ellipsometry results must be cross-correlated with other measurement techniques. To that end, the HR-STEM and APT analyses constitute a complementary analysis to SE to accurately estimate relevant parameters for the optical model like the periodicity m and the thicknesses of each layer in the SLs.

ASSOCIATED CONTENT

Supporting Information

The Supporting Information is available free of charge at <https://pubs.acs.org/doi/10.1021/acsami.9b13802>.

Additional experimental details; STEM and EELS: additional data; APT: additional data; Ellipsometry: key theoretical concepts; ellipsometry: additional data (PDF)

AUTHOR INFORMATION

Corresponding Authors

*E-mail: samik.mukherjee@polymtl.ca (S.M.).

*E-mail: oussama.moutanabbir@polymtl.ca (O.M.).

ORCID

Samik Mukherjee: 0000-0002-5279-1110

Oussama Moutanabbir: 0000-0002-0721-3696

Funding

This work was supported by NSERC Canada (Discovery, SPG, and CRD Grants), Canada Research Chairs, Canada Foundation for Innovation, Mitacs, PRIMA Québec, and Defence Canada (Innovation for Defence Excellence and Security, IDEaS).

Notes

The authors declare no competing financial interest.

REFERENCES

- (1) Dehlinger, G.; Diehl, L.; Gennser, U.; Sigg, H.; Faist, J.; Ensslin, K.; Grutzmacher, D.; Muller, E. Intersubband Electroluminescence from Silicon-Based Quantum Cascade Structures. *Science* **2000**, *290*, 2277–2280.
- (2) Maune, B. M.; Borselli, M. G.; Huang, B.; Ladd, T. D.; Deelman, P. W.; Holabird, K. S.; Kiselev, A. A.; Alvarado-Rodriguez, I.; Ross, R. S.; Schmitz, A. E.; Sokolich, M.; Watson, C. A.; Gyure, M. F.; Hunter, A. T. Coherent Singlet-Triplet Oscillations in a Silicon-Based Double Quantum Dot. *Nature* **2012**, *481*, 344–347.
- (3) Tan, K.-M.; Liow, T.-Y.; Lee, R. T. P.; Hoe, K. M.; Tung, C.-H.; Balasubramanian, N.; Samudra, G. S.; Yeo, Y.-C. Strained P-Channel FinFETs With Extended Π-Shaped Silicon–Germanium Source and Drain Stressors. *IEEE Electron Device Lett.* **2007**, *28*, 905–908.
- (4) Ciano, C.; Virgilio, M.; Montanari, M.; Persichetti, L.; Di Gaspare, L.; Ortolani, M.; Baldassarre, L.; Zoellner, M. H.; Skibitzki, O.; Scalari, G.; Faist, J.; Paul, D. J.; Scuderi, M.; Nicota, G.; Grange, T.; Birner, S.; Capelline, G.; Seta, M. De. Control of Electron-State Coupling in Asymmetric Ge/SiGe Quantum Wells. *Phys. Rev. Appl.* **2019**, *11*, No. 014003.
- (5) Presting, H. Near and Mid Infrared Silicon/Germanium Based Photodetection. *Thin Solid Films* **1998**, *321*, 186–195.
- (6) Rommel, S. L.; Dillon, T. E.; Dashiell, M. W.; Feng, H.; Kolodzey, J.; Berger, P. R.; Thompson, P. E.; Hobart, K. D.; Lake, R.; Seabaugh, A. C.; Klimeck, G.; Blanks, D. K. Room Temperature Operation of Epitaxially Grown Si/Si0.5Ge0.5/Si Resonant Interband Tunneling Diodes. *Appl. Phys. Lett.* **1998**, *73*, 2191.
- (7) Khurjin, J. B. Inhomogeneous Origin of the Interface Roughness Broadening of Intersubband Transitions. *Appl. Phys. Lett.* **2008**, *93*, No. 091104.
- (8) Lhuillier, E.; Ribet-Mohamed, I.; Rosencher, E.; Patriarche, G.; Buffaz, A.; Berger, V.; Carras, M. Interface Roughness Transport in Terahertz Quantum Cascade Detectors. *Appl. Phys. Lett.* **2010**, *96*, No. 061111.
- (9) Francké, M.; Winge, D. O.; Wolf, J.; Liverini, V.; Dupont, E.; Trinité, V.; Faist, J.; Wacker, A. Impact of Interface Roughness Distributions on the Operation of Quantum Cascade Lasers. *Opt. Express* **2015**, *23*, S201.
- (10) Krivas, K. A.; Winge, D. O.; Francké, M.; Wacker, A. Influence of Interface Roughness in Quantum Cascade Lasers. *J. Appl. Phys.* **2015**, *118*, No. 114501.
- (11) Hellings, G.; Mertens, H.; Subirats, A.; Simoen, E.; Schram, T.; Ragnarsdóttir, L.-A.; Simicic, M.; Chen, S.-H.; Parvais, B.; Boudier, D.; Cretu, B.; Machillot, J.; Pena, V.; Sun, S.; Yoshida, N.; Kim, N.; Mocuta, A.; Linten, D.; Horiguchi, N. In *Si/SiGe Superlattice I/O FinFETs in a Vertically-Stacked Gate-All-Around Horizontal Nanowire Technology*, 2018 IEEE Symposium on VLSI Technology; IEEE, 2018; pp 85–86.
- (12) Esaki, L.; Tsu, R. Superlattice and Negative Differential Conductivity in Semiconductors. *IBM J. Res. Dev.* **1970**, *14*, 61–65.
- (13) Koelling, S.; Gilbert, M.; Goossens, J.; Hikavyy, A.; Richard, O.; Vandervorst, W. High Depth Resolution Analysis of Si/SiGe Multilayers with the Atom Probe. *Appl. Phys. Lett.* **2009**, *95*, No. 144106.

- (14) Gredig, T.; Silverstein, E. A.; Byrne, M. P. Height-Height Correlation Function to Determine Grain Size in Iron Phthalocyanine Thin Films. *J. Phys. Conf. Ser.* **2013**, *417*, No. 012069.
- (15) Labat, S.; Guichet, C.; Thomas, O.; Gilles, B.; Marty, A. Microstructural Analysis of Au/NI Multilayers Interfaces by SAXS and STM. *Appl. Surf. Sci.* **2002**, *188*, 182–187.
- (16) Hellman, O. C.; Vandenbroucke, J. A.; Rüsing, J.; Isheim, D.; Seidman, D. N. Analysis of Three-Dimensional Atom-Probe Data by the Proximity Histogram. *Microsc. Microanal.* **2000**, *6*, 437–444.
- (17) Dyck, O.; Leonard, D. N.; Edge, L. F.; Jackson, C. A.; Pritchett, E. J.; Deelman, P. W.; Poplawsky, J. D. Accurate Quantification of Si/SiGe Interface Profiles via Atom Probe Tomography. *Adv. Mater. Interfaces* **2017**, *4*, No. 1700622.
- (18) Grützmacher, D. A.; Sedgwick, T. O.; Powell, A.; Tejwani, M.; Iyer, S. S.; Cotte, J.; Cardone, F. Ge Segregation in SiGe/Si Heterostructures and Its Dependence on Deposition Technique and Growth Atmosphere. *Appl. Phys. Lett.* **1993**, *63*, 2531–2533.
- (19) Tok, E.; Woods, N.; Zhang, J. RHEED and SIMS Studies of Germanium Segregation during Growth of SiGe/Si Heterostructures; a Two-Site Exchange Model with Growth Rate Dependence. *J. Cryst. Growth* **2000**, *209*, 321–326.
- (20) Ohtani, N.; Mokler, S.; Xie, M. H.; Zhang, J.; Joyce, B. A. Surface Hydrogen Effects on Ge Surface Segregation during Silicon Gas Source Molecular Beam Epitaxy. *Jpn. J. Appl. Phys.* **1994**, *33*, 2311–2316.
- (21) Aubertine, D. B.; Ozguven, N.; McIntyre, P. C.; Brennan, S. Analysis of X-Ray Diffraction as a Probe of Interdiffusion in Si/SiGe Heterostructures. *J. Appl. Phys.* **2003**, *94*, 1557–1564.
- (22) Aubertine, D. B.; Mander, M. A.; Ozguven, N.; Marshall, A. F.; McIntyre, P. C.; Chu, J. O.; Mooney, P. M. Observation and Modeling of the Initial Fast Interdiffusion Regime in Si/SiGe Multilayers. *J. Appl. Phys.* **2002**, *92*, 5027–5035.
- (23) Xie, M.-H.; Zhang, J.; Lees, A.; Fernandez, J. M.; Joyce, B. A. Surface Segregation during Molecular Beam Epitaxy: The Site-Blocking Effects of Surfactant Atoms. *Surf. Sci.* **1996**, *367*, 231–237.
- (24) Aspnes, D. E. Interface Ellipsometry; An Overview. *Surf. Sci.* **1980**, *101*, 84–98.
- (25) Aspnes, D. E. Optical Properties of Thin Films. *Thin Solid Films* **1982**, *89*, 249–262.
- (26) Freeouf, J. L. Application of Spectroscopic Ellipsometry to Complex Samples. *Appl. Phys. Lett.* **1988**, *53*, 2426–2428.
- (27) Nguyen, N. V.; Pellegrino, J. G.; Amirtharaj, P. M.; Seiler, D. G.; Qadri, S. B. Interface Roughness of Short-Period AlAs / GaAs Superlattices Studied by Spectroscopic Ellipsometry. *J. Appl. Phys.* **1993**, *73*, 7739–7746.
- (28) Ghong, T. H.; Kim, Y. D.; Aspnes, D. E.; Klein, M. V.; Ko, D. S.; Kim, Y. W.; Elarde, V.; Coleman, J. Interface Analysis of an AlGaAs Multilayer System by Using Spectroscopic Ellipsometry. *J. Korean Phys. Soc.* **2006**, *48*, 1601–1605.
- (29) Nolot, E.; Hartmann, J. M.; Hilfiker, J. Optical Constants Determination of Pseudomorphic $\text{Si}_{1-x}\text{Ge}_x$ Layers on Si(001), with $0 < x < 0.54$. *ECS Trans.* **2014**, *64*, 455–465.
- (30) Devaraj, A.; Perea, D. E.; Liu, J.; Gordon, L. M.; Prosa, T. J.; Parikh, P.; Diercks, D. R.; Meher, S.; Kolli, R. P.; Meng, Y. S.; Thevuthasan, S. Three-Dimensional Nanoscale Characterisation of Materials by Atom Probe Tomography. *Int. Mater. Rev.* **2017**, 1–34.
- (31) Mukherjee, S.; Watanabe, H.; Isheim, D.; Seidman, D. N.; Moutanabbir, O. Laser-Assisted Field Evaporation and Three-Dimensional Atom-by-Atom Mapping of Diamond Isotopic Homojunctions. *Nano Lett.* **2016**, *16*, 1335–1344.
- (32) Aspnes, D. E.; Studna, A. A. High Precision Scanning Ellipsometer. *Appl. Opt.* **1975**, *14*, 220–228.
- (33) Palik, E. D. *Handbook of Optical Constants of Solids*; Palik, E. D., Ed.; Academic Press: London, U.K., 1998.